Improvements of Critical Heat Flux Models Based on the Viscous Potential Flow Theory

Byoung Jae Kim[a*], Jong Hyuk Lee[a], Kyung Doo Kim[a]
[a]*Thermal-Hydraulic Safety Research Division, Korea Atomic Energy Research Institute.*
[*]*Corresponding author: byoungjae@kaeri.re.kr*

1. Introduction

During the review of the critical heat flux models for saturated pool boiling on infinite horizontal surfaces, we noticed that the effect of fluid viscosities is not included in most existing models. The absence of fluid viscosities in most existing models may be attributed to the fact that inviscid flow analyses are performed for the model development. For example, the hydrodynamic theory and macrolayer dryout models rely on the Rayleigh-Taylor, Kelvin-Helmholtz, and capillary instabilities for inviscid fluids. However, as the viscosities of two fluids become closer, none of them cannot be neglected. Moreover, the gas viscosity effect cannot be neglected on the condition that the gas layer is thin. Nevertheless, the previous studies neglected the viscous effect.

Recently, Kim et al. [1] showed that for the model development of critical heat flux and minimum film boiling, the Rayleigh-Taylor instability should be analyzed with a thin layer of viscous gas instead of a thick layer of inviscid gas. At to the most unstable wavelength, the case for two semi-infinite layers of inviscid fluids yields $\lambda_d = 2\pi(3\sigma/(\Delta\rho g))^{1/2}$, whereas the case for a thin layer of viscous gas underlying a semi-infinite layer of viscous liquid gives $\lambda_d = 2\pi(2\sigma/(\Delta\rho g))^{1/2}$, where σ, $\Delta\rho$, and g are the surface tension, density difference between liquid and gas, and gravitational acceleration, respectively. The decrease of the most unstable wavelength was shown to improve the prediction accuracy of critical heat flux models for various fluids, particularly at elevated pressures. In addition, the most dangerous wavelength and the most rapid growth rate for viscous thin films are shown to be applicable to the minimum heat flux condition.

Kim et al. [1] touch only the most unstable wavelength for developing critical heat flux models. The critical heat flux is inversely proportional to the square root of the most unstable wavelength (Zuber [2], Guan et al. [3]). Here, we notice that the existing critical heat flux models make use of the Kelvin-Helmholtz instability of inviscid flows. The Kelvin-Helmholtz instability determines the maximum vapor escape velocity (Zuber [2]) and the initial liquid macrolayer thickness (Haramura and Katto [4]). Therefore, there is a room for improving the prediction accuracy by the help of the Kelvin-Helmholtz instability of viscous fluids.

The Kelvin-Helmholtz instability arises when the different fluid layers are in relative motion. Usually, a uniform flow is considered in each fluid layer, allowing a velocity discontinuity at the interface. Therefore, in general, the Kelvin-Helmholtz instability is analyzed based on a potential flow of inviscid fluids. However, if the viscosity effect is taken into consideration, a non-uniform flow occurs due to the shear stress at the interface. The idea to incorporate the effects of fluid viscosities into the Kelvin-Helmholtz instability can be found in the viscous potential flow theory.

Joseph and Liao [5] showed that the potential (irrotational) flow of viscous fluids satisfies the Navier-Stokes equation. For the potential flow, since the vorticity is identically zero, the viscous term vanishes in the Navier-Stokes equation; the motion of fluid is governed by the Bernoulli equation. However, the viscous stresses do not vanish in general. Therefore, the viscous pressure is entered through the normal stress balance at the interface. In the viscous potential flow, the shear stress is neglected at the interface and wall, and thus there is a velocity slip at the interface. These treatments are consistent with the fact that the interface waves are induced more by pressure than by shear force. Funada and Joseph [6] presented a viscous potential flow analysis of the Kelvin-Helmholtz instability. Funada et al. [7] carried out a stability analysis of a circular fluid jet into another fluid. Funada and Joseph [8] considered the capillary instability. The viscous potential flow analysis is more accurate than the inviscid flow analysis in terms of the growth rate. Therefore, the critical condition of the Kelvin-Helmholtz instability can be predicted more accurately than the inviscid flow analysis.

In this study, the interfacial instabilities of viscous potential flows are applied to critical heat flux models for saturated pool boiling on infinite horizontal surfaces, with the aim of including the effects of fluid viscosities. The critical conditions of the circular jet and Kelvin-Helmholtz instabilities are incorporated into the hydrodynamic theory model and liquid macrolayer dryout model.

2. Interfacial Instabilities of Viscous Potential Flow

2.1Kevin-Helmholtz Instability

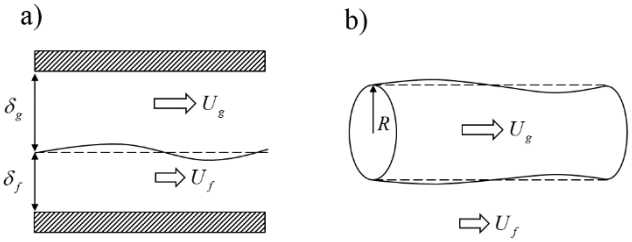

Fig. 1 a) Two fluid layers with different densities move parallel to each other in a 2D channel. b) A circular gas jet issues into a liquid.

Funada and Joseph [6] presented the Kelvin-Helmholtz instability (Fig. 1a). Let U_g and U_f be the gas and liquid velocities, respectively. Hereafter, the gas and liquid are denoted by g and f, respectively. If the gravity effect is ignored, which is reasonable because the vapor jet issues upward, the critical relative velocity $U_c = U_g - U_f$ is given by

$$U_c^2 = \left[\frac{\tanh(k_c\delta_g)}{\rho_g} + \frac{\tanh(k_c\delta_f)}{\rho_f} \right] \sigma k_c \qquad (1)$$

for inviscid potential fluids, and

$$U_c^2 = \frac{\sigma k_c \left[\mu_g \coth(k_c\delta_g) + \mu_f \coth(k_c\delta_f) \right]^2}{\rho_g \mu_f^2 \coth(k_c\delta_g)\coth^2(k_c\delta_f) + \rho_f \mu_g^2 \coth(k_c\delta_f)\coth^2(k_c\delta_g)} \qquad (2)$$

for viscous potential fluids, where ρ, μ, δ, and k_c are the density, viscosity, fluid layer thickness, and critical wavenumber, respectively.

2.2 Circular Jet Instability

Funada et al. [7] carried out a stability analysis for a circular fluid jet into another fluid (Fig. 1b). If the relative velocity between the jet and the surrounding fluid is zero, the situation is the same as the capillary instability. On the other hand, as the relative velocity increases, the jet undergoes the Kelvin-Helmholtz instability. Only a gas jet into a liquid is considered here. The critical relative velocity is given by

$$U_c^2 = \frac{\sigma(\alpha_g\rho_g + \alpha_f\rho_f)}{\alpha_g\alpha_f\rho_g\rho_f}\left(k_c - \frac{1}{R^2 k_c} \right) \qquad (3)$$

for inviscid potential fluids, and

$$U_c^2 = \frac{\sigma(\beta_g\mu_g + \beta_f\mu_f)^2}{\alpha_g\rho_g\beta_f^2\mu_f^2 + \alpha_f\rho_f\beta_g^2\mu_g^2}\left(k_c - \frac{1}{R^2 k_c} \right) \qquad (4)$$

for viscous potential fluids, where R is the gas jet diameter. The non-dimensional variables α_g, α_f, β_g, and β_f are defined as

$$\alpha_g = \frac{I_0(Rk_c)}{I_1(Rk_c)}, \quad \alpha_f = \frac{K_0(Rk_c)}{K_1(Rk_c)}, \qquad (5)$$

$$\beta_g = \alpha_g - \frac{1}{Rk_c}, \quad \beta_f = \alpha_f + \frac{1}{Rk_c}. \qquad (6)$$

where I_0 and I_1 are the modified Bessel functions of the first kind, and K_0 and K_1 are the modified Bessel functions of the second kind. For large jet diameters, α_g, α_f, β_g, and β_f approach unity. In this case, Eq. (3) and (4), respectively, become close to Eq. (1) and (2) with large δ_g and δ_f. In other words, circular jets with large diameters can be analyzed by the Kelvin-Helmholtz instability with large fluid thicknesses.

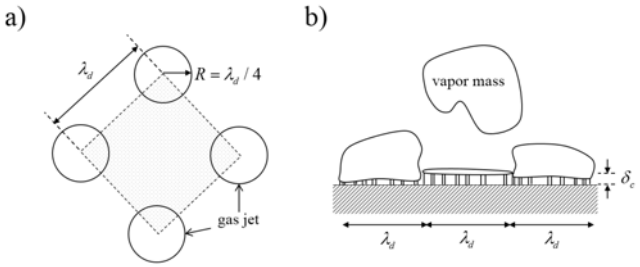

Fig. 2 Schematics of pool boiling critical heat flux models on infinite horizontal surfaces: a) Hydrodynamic instability model (top view of rising jets); b) Liquid macrolayer dryout model (side view of rising vapor masses).

3. Revised Critical Heat Flux Models

2.1 Hydrodynamic Model

Zuber [2] developed a critical heat flux model, assuming that circular vapor jets rise at the nodes of Taylor waves and that the jet diameter is half of the jet spacing (Fig. 2a). As a result, the critical heat flux was formulated as

$$q_{\max} = \frac{\pi}{16}\rho_g L U_g, \qquad (7)$$

where U_g is the maximum gas velocity which corresponds to the critical condition of the Kelvin-Helmholtz instability. The critical relative velocity for an inviscid flow is

$$U_c = U_g - U_f = \left(\frac{2\pi\sigma}{\lambda_c}\frac{\rho_g + \rho_f}{\rho_g\rho_f} \right)^{1/2}, \qquad (8)$$

where λ_c is the critical wavelength. Zuber`s choice for λ_c was the critical wavelength of capillary waves: $\lambda_c = 2\pi R$, where R is the radius of circular gas jets. As a consequence, Zuber obtained

$$\frac{q_{\max}}{\rho_g^{1/2} L(\sigma\Delta\rho g)^{1/4}} = \frac{\pi}{24}\frac{(16-\pi)\rho_f}{\pi\rho_g + (16-\pi)\rho_f}\left(\frac{\rho_f + \rho_g}{\rho_f} \right)^{1/2}, \qquad (9)$$

where L is the latent heat. At low pressures, the above equation is approximated as

$$\frac{q_{\max}}{\rho_g^{1/2} L(\sigma\Delta\rho g)^{1/4}} = 0.131. \qquad (10)$$

An inconsistency is pointed out in Zuber`s model. Equation (8) is the result of the Kelvin-Helmholtz instability. However, the choice for λ_c in Eq. (8) is the critical wavelength of standing capillary waves. Note that $\lambda_c = 2\pi R$ (or $k_c = 1/R$) leads to $U_c = U_g - U_f = 0$ for circular gas jets, as shown in Eqs. (3) and (4). This means that the vapor velocity is zero in pool boiling, and thus the critical heat flux becomes zero.

To avoid this unphysical assumption, the instability analysis for circular gas jets must be utilized. As Zuber [2] did, let us first assume $R = \lambda_d / 4$, where λ_d is the

most unstable wavelength of the Rayleigh-Taylor instability. Using the conservation of mass,

$$U_f = -\frac{\pi}{16-\pi}\frac{\rho_g}{\rho_f}U_g \,. \tag{11}$$

For an inviscid flow, Eq. (3) is combined with Eq. (11) to give

$$U_g = \frac{(16-\pi)\rho_f}{\pi\rho_g + (16-\pi)\rho_f}\left[\frac{\sigma(\alpha_g\rho_g + \alpha_f\rho_f)}{\alpha_g\alpha_f\rho_g\rho_f}\left(k_c - \frac{16}{\lambda_d^2 k_c}\right)\right]^{1/2} . \tag{12}$$

Upon substituting of this into Eq. (7), we have

$$q_{\max} = \frac{\pi}{16}\left(k_c - \frac{16}{\lambda_d^2 k_c}\right)^{1/2}\frac{(16-\pi)\rho_f}{\pi\rho_g + (16-\pi)\rho_f}\rho_g^{1/2}L \times\left[\frac{\sigma(\alpha_g\rho_g + \alpha_f\rho_f)}{\alpha_g\alpha_f\rho_f}\right]^{1/2} . \tag{13}$$

The most unstable wavelength λ_d is given by the Rayleigh-Taylor instability. There is a drawback of the Rayleigh-Taylor instability of the viscous potential flow. As the thickness of the gas layer decreases to the extent of creeping flow, the most unstable wavelength tends to increase unboundedly though the fastest growth rate may become accurate (Kim et al. [1]). Therefore, when the gas layer is thin, either fully viscous flow analysis or lubrication approximation should be made. In those analyses, λ_d is given by $2\pi(2\sigma/(\Delta\rho g))^{1/2}$ for a thin layer of gas. The critical wavenumber k_c is supposed to be $\gamma(\Delta\rho g/\sigma)^{1/2}$. Then, we can write Eq. (13) as

$$\frac{q_{\max}}{\rho_g^{1/2}L(\sigma\Delta\rho g)^{1/4}} = \frac{\pi}{16}\left(\gamma - \frac{2}{\pi^2\gamma}\right)^{1/2}\frac{(16-\pi)\rho_f}{\pi\rho_g + (16-\pi)\rho_f} \times\left[\frac{(\alpha_g\rho_g + \alpha_f\rho_f)}{\alpha_g\alpha_f\rho_f}\right]^{1/2} . \tag{14}$$

For large jet diameters such that α_g and α_f settle to unity, the above equation reduces to the form of Eq. (9).

Now let us consider a viscous potential flow. Equation (4) is combined with Eq. (11) to give

$$U_g = \frac{(16-\pi)\rho_f}{\pi\rho_g + (16-\pi)\rho_f} \times\left[\frac{\sigma(\beta_g\mu_g + \beta_f\mu_f)^2}{\alpha_g\rho_g\beta_f^2\mu_f^2 + \alpha_f\rho_f\beta_g^2\mu_g^2}\left(k_c - \frac{16}{\lambda_d^2 k_c}\right)\right]^{1/2} . \tag{15}$$

Substituting this into Eq. (7) and using $\lambda_d = 2\pi(2\sigma/(\Delta\rho g))^{1/2}$ and $\gamma(\Delta\rho g/\sigma)^{1/2}$, we obtain

$$\frac{q_{\max}}{\rho_g^{1/2}L(\sigma\Delta\rho g)^{1/4}} = \frac{\pi}{16}\left(\gamma - \frac{2}{\pi^2\gamma}\right)^{1/2} \times\frac{(16-\pi)\rho_f}{\pi\rho_g + (16-\pi)\rho_f}\frac{\rho_g^{1/2}(\beta_g\mu_g + \beta_f\mu_f)}{(\alpha_g\rho_g\beta_f^2\mu_f^2 + \alpha_f\rho_f\beta_g^2\mu_g^2)^{1/2}} . \tag{16}$$

This is the revised hydrodynamic model based on the viscous potential flow. Yagov [9] stated that if one considers only the surface tension and body forces, one inevitably obtains an equation similar to Eq. (9) in view of a dimensional analysis. In fact, most of the critical heat flux models only replace the right-hand side of Eq. (9) by values that are functions of the liquid-gas density ratio. However, it is noteworthy that Eq. (16) includes liquid and gas viscosities. Unknown parameters will be determined in the next chapter.

2.3 Liquid Macrolayer Dryout Model

Haramura and Katto [4] postulated that critical heat flux occurs when the liquid macrolayer under the massive vapor bubble evaporates away during the hovering time of the overlying vapor mass (Fig. 2b).

$$q_{\max} = \rho_f\delta_c L(1 - A_g/A_w)f \,, \tag{17}$$

where δ_c, A_g, A_w, and f are the initial macrolayer thickness, total bottom area of vapor stems, area of the heated surface, and bubble detachment frequency, respectively. The bubble detachment frequency was related to the motion of a growing bubble from the heater surface. The initial macrolayer thickness was assumed to be $\delta_c = \lambda_{c,\mathrm{ipf}}/4$, where $\lambda_{c,\mathrm{ipf}}$ is the critical wavelength of the Kelvin-Helmholtz instability for inviscid potential flows:

$$\lambda_{c,\mathrm{ipf}} = 2\pi\sigma\frac{\rho_g + \rho_f}{\rho_g\rho_f}\left(\frac{A_g}{A_w}\right)^2\left(\frac{\rho_g L}{q_{\max}}\right)^2 . \tag{18}$$

With the above assumptions, Haramura and Katto [4] obtained

$$\frac{q_{\max}}{\rho_g^{1/2}L(\sigma\Delta\rho g)^{1/4}} = \left(\frac{\pi^4}{2^{11}\cdot 3^2}\right)^{1/16}\left(\frac{A_g}{A_w}\right)^{5/8}\left(1 - \frac{A_g}{A_w}\right)^{5/16} \times\left(1 + \frac{\rho_f}{\rho_g}\right)^{5/16}\left(\frac{11}{16}\frac{\rho_f}{\rho_g} + 1\right)^{-3/16} , \tag{19}$$

and equated the right-hand side to the value of 0.131, giving

$$A_g/A_w = 0.0584(\rho_g/\rho_f)^{0.2} . \tag{20}$$

Now, the results of instabilities of viscous potential flows are applied to the dryout model. A summary is described below. The critical wavelength for the Kelvin-Helmholtz instability is given by

$$\lambda_{c,\mathrm{vpf}} = 2\pi\sigma\frac{(\mu_g + \mu_f)^2}{\rho_g\mu_f^2 + \rho_f\mu_g^2}\left(\frac{A_g}{A_w}\right)^2\left(\frac{\rho_g L}{q_{\max}}\right)^2 . \tag{21}$$

The liquid macrolayer thickness is assumed to be $\delta_c = \eta\lambda_{c,\mathrm{vpf}} = \eta(2\pi/k_c)$. The liquid macrolayer thickness is calculated using the correlation by Rajvanshi et al. [10]. Consequently, we obtain

$$\frac{q_{\max}}{\rho_g^{1/2}L(\sigma\Delta\rho g)^{1/4}} = \left(\frac{\eta^5\pi^4}{2\cdot 3^2}\right)^{1/16}\left(\frac{A_g}{A_w}\right)^{5/8}\left(1 - \frac{A_g}{A_w}\right)^{5/16} \times\left(\frac{\rho_f(\mu_g + \mu_f)^2}{\rho_g\mu_f^2 + \rho_f\mu_g^2}\right)^{5/16}\left(\frac{11}{16}\frac{\rho_f}{\rho_g} + 1\right)^{-3/16} , \tag{22}$$

where

$$\eta = \frac{1}{2}\frac{\rho_g + \rho_f}{\rho_g \rho_f}\frac{\rho_g \mu_f^2 + \rho_f \mu_g^2}{(\mu_g + \mu_f)^2}, \quad (23)$$

$$\frac{A_g}{A_w} = 0.0413\eta^{-1/2}\left(1+\frac{\rho_g}{\rho_f}\right)^{1/2}\left(\frac{\rho_g}{\rho_f}\right)^{1/5}\left(\frac{\rho_g \mu_f^2 + \rho_f \mu_g^2}{\rho_g(\mu_g+\mu_f)^2}\right)^{1/2}. \quad (24)$$

4. Results and Discussion

There is only one unknown parameter γ in Eqs. (14) and (16) because α_g, α_f, β_g, and β_f are linked to γ through $k_c = \gamma\left(\Delta\rho g/\sigma\right)^{1/2}$. Lienhard and Dhir [11] noticed that Eq. (9) slightly under-predicts the experimental data of various liquids. They modified the numerical constant as follows:

$$\frac{q_{\max}}{\rho_g^{1/2} L(\sigma\Delta\rho g)^{1/4}} = 0.149\frac{(16-\pi)\rho_f}{\pi\rho_g + (16-\pi)\rho_f}\left(\frac{\rho_f+\rho_g}{\rho_f}\right)^{1/2}. \quad (25)$$

We rely on the accuracy of Eq. (25) at atmospheric pressure. It is now postulated that at atmospheric pressure, the right-hand sides of Eqs. (14)and (16) equal the right-hand side of Eq. (25). The value of γ was numerically solved for various liquids, and the results are provided in Table 1. Interestingly, γ does not vary significantly from fluid to fluid, except for water.

Figure 3 compares the predictions by Eqs. (14) and (16) with experimental data of water. The models of Zuber [2] (Eq. (9)), Lienhard and Dhir [11] (Eq. (25)), and Yagov [9] are also plotted in the figure. The model of Yagov [9] is the one for moderate and elevated pressures: $q_{\max} = 0.06L\rho_g^{0.6}\sigma^{0.4}(\Delta\rho g/\mu_f)^{0.2}$. The lines are the predictions by the models, and the symbols are the experimental data. Indistinguishable differences are seen between Eqs. (14) and (25), which may be attributed to the fact that they are based on inviscid flows. However, the prediction accuracy of Eq. (16) is greatly improved at moderate and elevated pressures. The inclusion of viscosities contributes to such improvement. From now, only the models based on the viscous potential flow will be considered.

Figure 4 shows a comparison of the revised macrolayer dryout model, Eq. (22), with experimental data of water. The values predicted by Haramura and Katto [4] are the same as those by Zuber [2]. As mentioned previously, only the difference between the present work and Haramura and Katto [4] is the use of (21) instead of Eq. (18). This difference leads to improved predictions in Fig. 4. Sakashita and Ono [12] developed a semi-empirical correlation for the bubble detachment frequency of water boiling at elevated pressures, and they applied it to the liquid macrolayer dryout model. The predictions marked by Sakashita and Ono [12] in Fig. 4 show considerable over-predictions at low pressures.

Recall that γ, α_g, α_f, β_g, and β_f in Table 1 are close to one another, except water. The averaged values of five liquids except water ($\gamma = 1.01$, $\alpha_g = 1.36$, $\alpha_f = 0.832$, $\beta_g = 0.915$, $\beta_f = 1.27$) are used to predict the critical heat flux for those liquids using the revised hydrodynamic model in Eq. (16). Figures 5 through 9 show the comparison results for organic fluids. In the figures, predictions marked by the present (hydrodynamic) and present (macrolayer), respectively, correspond to the revised hydrodynamic model in Eq. (16), and the revised macrolayer model in Eq. (22). Unlike water, the predicted values from the revised macrolayer model are higher than those from the revised hydrodynamic model. For organic fluids, at a glance, the revised models show prediction accuracies similar to Lienhard and Dhir [11]. The prediction accuracies are not improved as much as in water. One of reasons may be attributed to the high viscosity ratios for organic fluids. Figure 10 shows the ratio of the liquid viscosity to the vapor viscosity depending on the pressure. As seen, the viscosity ratio is the lowest for water. As the vapor and liquid viscosities become closer, none of them cannot be neglected. However, for the other organic fluids, the vapor viscosity is considerably lower than the liquid viscosity. In this case, the effect of the vapor viscosity diminishes, and the inclusion of the viscosity may not be effective than expected. Nevertheless, the advantage of the revised models consist in the inclusion of the effect of fluid viscosities.

5. Conclusions

Circular jet instabilities is incorporated into the hydrodynamic theory model. For water, the circular jet instability of an inviscid potential flow does not show any improvement of the prediction accuracy over the existing model, whereas the circular jet instability of a viscous potential flow shows a considerable improvement particularly at elevated pressures. There is one unknown variable in the revised hydrodynamic model. Interestingly, the variable is shown to vary little from fluid to fluid, except for water. Meanwhile, the Kelvin-Helmholtz instability of a viscous potential flow is used to determine the initial macrolayer thickness in the liquid macrolayer model. The revised macrolayer model shows improved predictions as accurate as Lienhard and Dhir [11]. By the inclusion of the effects of fluid viscosities, the models become, on the whole, more accurate than the models based on inviscid potential flows.

Table 1. Parameters in Eq. (13) and (16)

Fluid	Equation	γ	α_g	α_f	β_g	β_f
Water	Eq. (13)	0.994	1.372	0.828	-	-
	Eq. (16)	1.640	1.179	0.885	0.904	1.160
Methanol	Eq. (16)	1.081	1.326	0.839	0.910	1.255
Hexane	Eq. (16)	1.013	1.361	0.830	0.916	1.275
R113	Eq. (16)	0.996	1.370	0.828	0.918	1.280
Pentane	Eq. (16)	1.012	1.361	0.830	0.916	1.275
Ethanol	Eq. (16)	1.017	1.358	0.831	0.916	1.273

Acknowledgement

This work was supported by the Nuclear Power Technology Development Program of the Korea Institute of Energy Technology Evaluation and Planning (KETEP) grant funded by the Korea Government Ministry of Knowledge Economy (MKE). This work was also supported by the Nuclear Safety Research Center Program of the KORSAFe grant (Grant Code 1305011) funded by Nuclear Safety and Security Commission of the Korean

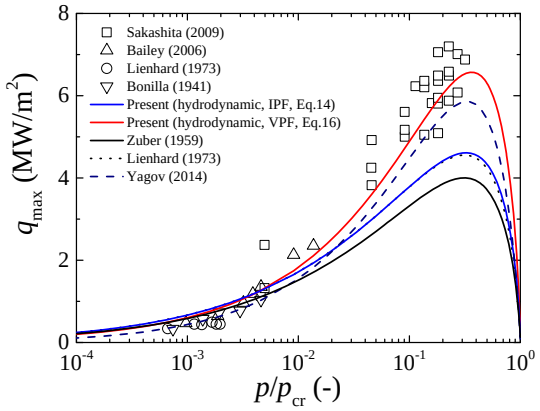

Fig. 3 Comparison of the revised hydrodynamic models with experimental data of water. Eq. (14): inviscid potential flow (blue line), Eq. (16): viscous potential flow (red line)

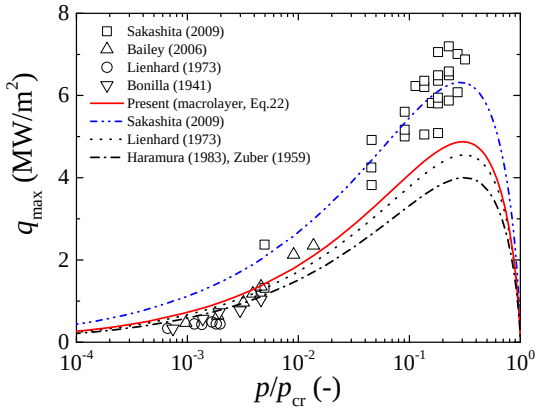

Fig. 4 Comparison of the revised macrolayer model, Eq. (22), with experimental data of water.

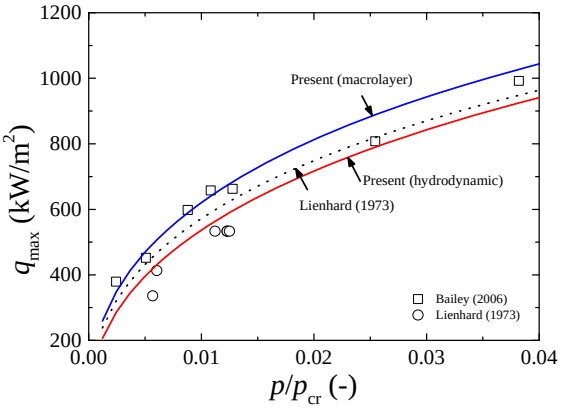

Fig. 5 Comparison of the revised models based on viscous potential flow with experimental data for methanol.

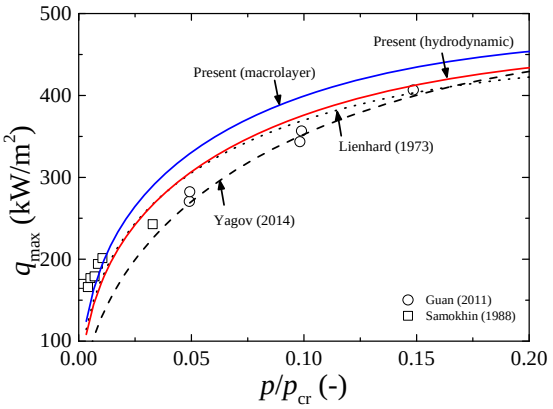

Fig. 6 Comparison of the revised models based on viscous potential flow with experimental data for hexane.

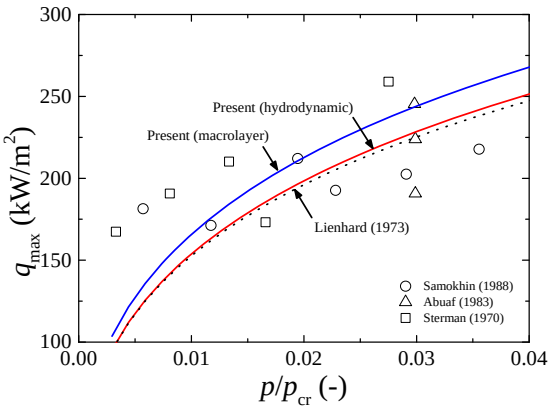

Fig. 7 Comparison of the revised models based on viscous potential flow with experimental data for R113.

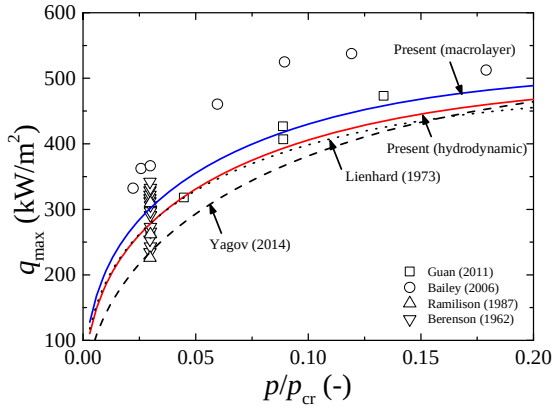

Fig. 8 Comparison of the revised models based on viscous potential flow with experimental data for pentane.

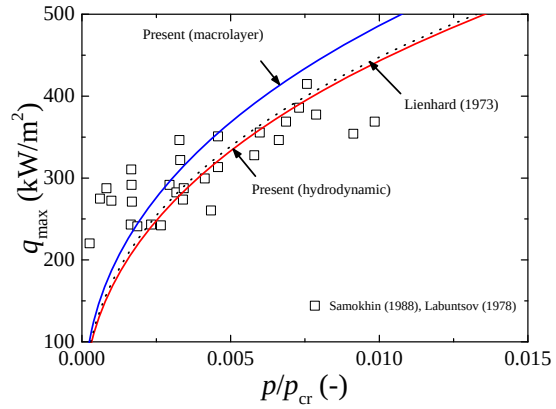

Fig. 9 Comparison of the revised models based on viscous potential flow with experimental data for ethanol.

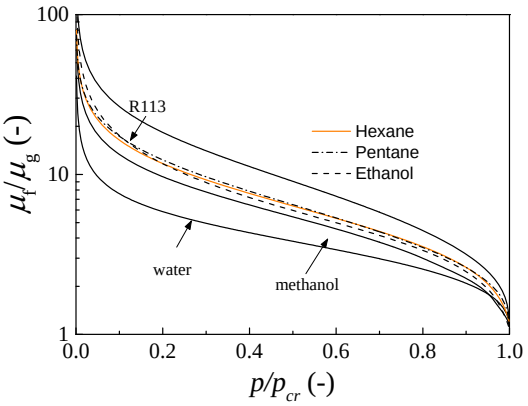

Fig. 10 Variations of the viscosity ratios with the pressure.

REFERENCES

[1] B.J. Kim, J.H. Lee, K.D. Kim, Rayleigh-taylor instability for thin gas films: Application to critical heat flux and minimum film boiling, International Journal of Heat and Mass Transfer 80 (2015) 150-158.

[2] N. Zuber, Hydrodynamic aspects of boiling heat transfer, Ph.D. Thesis, University of California, Los Angeles, USA, 1959.

[3] C.-K. Guan, J.F. Klausner, R. Mei, A new mechanistic model for pool boiling chf on horizontal surfaces, International Journal of Heat and Mass Transfer 54 (17–18) (2011) 3960-3969.

[4] Y. Haramura, Y. Katto, A new hydrodynamic model of critical heat flux, applicable widely to both pool and forced convection boiling on submerged bodies in saturated liquids, International Journal of Heat and Mass Transfer 26 (3) (1983) 389-399.

[5] D.D. Joseph, T.Y. Liao, Potential flows of viscous and viscoelastic fluids, Journal of Fluid Mechanics 265 (1994) 1-23.

[6] T. Funada, D.D. Joseph, Viscous potential flow analysis of kelvin–helmholtz instability in a channel, Journal of Fluid Mechanics 445 (2001) 263-283.

[7] T. Funada, D.D. Joseph, S. Yamashita, Stability of a liquid jet into incompressible gases and liquids, International Journal of Multiphase Flow 30 (11) (2004) 1279-1310.

[8] T. Funada, D.D. Joseph, Viscous potential flow analysis of capillary instability, International Journal of Multiphase Flow 28 (9) (2002) 1459-1478.

[9] V.V. Yagov, Is a crisis in pool boiling actually a hydrodynamic phenomenon?, International Journal of Heat and Mass Transfer 73 (0) (2014) 265-273.

[10] A.K. Rajvanshi, J.S. Saini, R. Prakash, Investigation of macrolayer thickness in nucleate pool boiling at high heat flux, International Journal of Heat and Mass Transfer 35 (2) (1992) 343-350.

[11] J.H. Lienhard, V.K. Dhir, Extended hydrodynamic theory of the peak and minimum pool boiling heat fluxes, NASA CR-2270, NASA, USA, 1973.

[12] H. Sakashita, A. Ono, Boiling behaviors and critical heat flux on a horizontal plate in saturated pool boiling of water at high pressures, International Journal of Heat and Mass Transfer 52 (3–4) (2009) 744-750.

[13] C.F. Bonilla, C.W. Perry, Heat transmission to boiling binary liquid mixtures, Transactions of American Society of Chemical Engineers 41 (1941) 755-787.

[14] G.I. Samokhin, V.V. Yagov, Heat transfer and critical heat fluxes with liquids boiling in the region of low reduced pressures, Thermal Engineering (English translation of Teploenergetika) 35 (1988) 746-752.

[15] L.S. Sterman, J. Korychanek, Critical heat fluxes during boiling of high-boiling heat carriers, Soviet Atomic Energy 29 (5) (1970) 1124-1125.

[16] N. Abuaf, F.W. Staub, Low pressure pool boiling and critical heat flux limits for r-113, AIChE Symposium series 79 (225) (1983) 35-40.

[17] P.J. Berenson, Experiments on pool-boiling heat transfer, International Journal of Heat and Mass Transfer 5 (10) (1962) 985-999.

[18] J.M. Ramilison, J.H. Lienhard, Transition boiling heat transfer and the film transition regime, Journal of Heat Transfer 109 (3) (1987) 746-752.

[19] D.A. Labuntsov, About a new approach in boiling crisis theory, Thermal Engineering (English translation of Teploenergetika) 8 (1961) 81-85.